

Structure and magnetic properties of $\text{Ni}_4\text{V}_3\text{O}_{10}$, an antiferromagnet with three types of vanadium-oxygen polyhedra

Zachary W. Riedel,^{†,‡} Fatemeh Amerikheirabadi,^{¶,‡} Kejian Qu,^{¶,‡} Jeffrey Huang,^{†,‡} Mebatsion S. Gebre,^{†,‡} Ankita Bhutani,^{†,‡} Richard T. Haasch,[‡] Pinshane Y. Huang,^{†,‡} André Schleife,^{†,‡,§} and Daniel P. Shoemaker^{*,†,‡}

[†]*Department of Materials Science and Engineering, University of Illinois at Urbana-Champaign, Urbana, Illinois 61801, United States*

[‡]*Materials Research Laboratory, University of Illinois at Urbana-Champaign, Urbana, Illinois 61801, United States*

[¶]*Department of Physics, University of Illinois at Urbana-Champaign, Urbana, Illinois 61801, United States*

[§]*National Center for Supercomputing Applications, University of Illinois at Urbana-Champaign, Urbana, IL 61801, United States*

E-mail: dpshoema@illinois.edu

Abstract

The compound $\text{Ni}_4\text{V}_3\text{O}_{10}$ forms a new structure type in the tetragonal space group $P4/n$. The material can be produced using solid-state synthesis in a narrow temperature range, and the structure was confirmed using X-ray and neutron powder diffraction data. The phase contains occupationally disordered Ni/V in tetrahedral, square pyramidal, and octahedral sites. Bond valence and neutron/X-ray co-refinements give evidence for three vanadium oxidation states (V^{3+} , V^{4+} , V^{5+}), making it distinct in the Ni–V–O system and placing it in a class of only nine other oxides with transition metals exhibiting three oxidation states. With a Néel temperature of 38 K and a Curie-Weiss parameter $\theta = -234$ K, it displays frustrated antiferromagnetism, evidenced by a broad hump in the heat capacity below T_N . The structure has a percolating distorted rock-salt-like network, leading to strong superexchange, but square pyramidal linkages frustrate magnetic ordering. The magnetic struc-

ture is assumed to be incommensurate, as simple propagation vectors can be ruled out by powder neutron diffraction.

Keywords

magnetic properties, solid-state structures, solid-state synthesis, antiferromagnet, diffraction

Introduction

The Ni–V–O chemical system contains multiple ternary compounds with intriguing magnetic and electronic properties. $\text{Ni}_3\text{V}_2\text{O}_8$ forms a Kagomé staircase structure with four low-temperature magnetic transitions^{1,2} and has emerged as a component in new supercapacitors.^{3–6} Both NiV_3O_8 , a ferromagnet with transitions at 2 and 27 K,⁷ and $\text{Ni}_2\text{V}_2\text{O}_7$, a 3D spin-1 antiferromagnet,⁸ have shown promising electrochemical properties for Li-ion battery

applications.^{9–12} Likewise, NiVO_3 and NiV_2O_6 have demonstrated high, stable discharge capacities as anode materials in Li-ion batteries.^{13,14} As a result, Li *et al.* have proposed using NiV_2O_6 as an electrode for flexible energy storage devices in wearable technology.¹⁵ Another compound in the system, hematite-type $\text{V}_{2-x}\text{Ni}_x\text{O}_3$ ($0 < x < 0.75$), is a wide solubility limit magnetic material with a tunable Mott transition temperature.^{16,17} These phases are plotted in Fig. 1.

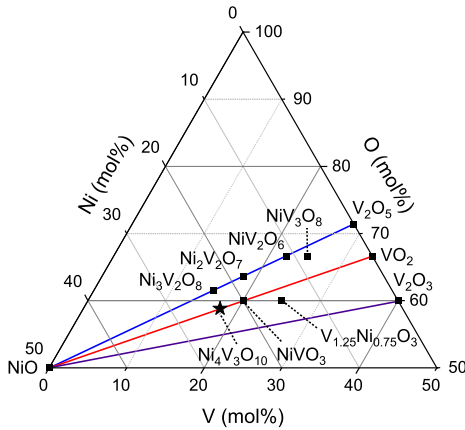


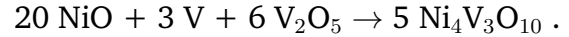
Figure 1: Truncated Ni-V-O phase diagram containing experimental phases near the composition of $\text{Ni}_4\text{V}_3\text{O}_{10}$. Lines indicate constant vanadium oxidation states (purple: V^{3+} , red: V^{4+} , blue: V^{5+}).

Gianoglio and Ramonda reported an additional ternary phase close to these others in composition and designated it as $\text{Ni}_7\text{V}_5\text{O}_{17}$ based on their reactant powders’ nominal Ni:V ratio and vanadium oxidation state.¹⁸ While d -spacings and relative intensities from X-ray diffraction data were reported for the new phase, its composition was not confirmed, the crystal structure was not determined, and the magnetic properties were not explored. Here, we show this phase to have an approximate composition of $\text{Ni}_4\text{V}_3\text{O}_{10}$, a unique structure type, and frustrated antiferromagnetic ordering.

Experimental Procedure

Synthesis

The precursor powder mixture for $\text{Ni}_4\text{V}_3\text{O}_{10}$ was prepared using two methods: high impact mechanical ball milling or hand grinding with an agate mortar and pestle. For samples prepared using ball milling, a total of 2 g of powder of NiO (Alfa Aesar, 99%), V (Strem, 99.5%), and V_2O_5 (Acros, 99.6%) were mixed under Ar in a stoichiometric ratio based on the chemical equation



Three stainless steel milling balls were used, with diameters of 0.5, 0.25, and 0.25 inches and with a combined mass of 10 g. The powders were sealed under Ar in a stainless steel jar and were milled for 1 h in a SPEX 8000D mixer mill under Ar. Next, the powders were dry pressed at 465 MPa into pellets and loaded into a short quartz tube that was placed into a larger tube. During the subsequent vacuum sealing, this tube-in-tube design prevented contact between the heated quartz and V powder, which hardens the tube. Samples were then heated at $10^\circ\text{C}/\text{min}$ to 800°C where they were held for 72 h before quenching in an ice bath.

Samples were also prepared without ball milling. Using a mortar and pestle, a total of 2 g of the same precursor powders in the same proportions were ground together for 45 min under Ar. They were then pressed and sealed as before. After ramping to 800°C at $10^\circ\text{C}/\text{min}$, they were held for 144 h before being quenched in an ice bath. Pellets were then ground before repeating the pressing and sealing process. The new tube was then placed in a preheated, 800°C oven. Three 144 h cycles were completed.

Additionally, to disentangle the effects of any hematite-type $(\text{V,Ni})_2\text{O}_3$ impurities in the title compound, the impurity phase was synthesized using the same precursor powders in an approximate NiO:V: V_2O_5 molar ratio of 335:199:233 ($\text{V}_{1.33}\text{Ni}_{0.67}\text{O}_3$). The powders, totalling 0.5 g, were hand ground with a mortar

and pestle under Ar before dry pressing and sealing in a quartz tube under vacuum. The sample was heated at 10°C/min to 950°C, the same temperature used by Rozier *et al.*,¹⁷ for 48 h before cooling naturally with the furnace over roughly 3 h.

Characterization

Room temperature X-ray powder diffraction data were collected at the Advanced Photon Source beamline 11-BM at Argonne National Laboratory ($\lambda = 0.457913$ Å). Time-of-flight neutron powder diffraction data were collected at the POWGEN instrument at Oak Ridge National Laboratory’s Spallation Neutron Source. Data collection occurred at 300 K and 6.4 K with additional data collected during cooling from 80 K to 9 K at 0.8 K/min.

The crystal structure of $\text{Ni}_4\text{V}_3\text{O}_{10}$ was initially solved using the parallel tempering global optimization algorithm in FOX¹⁹ with the 11-BM X-ray powder diffraction data. Rietveld refinements to X-ray and neutron powder diffraction data were performed with GSAS-II.²⁰ The Bilbao Crystallographic Server’s PSEUDO²¹ program guided crystallographic space group determination, and the server’s MAXMAGN²² program provided the maximal magnetic space groups for $\text{Ni}_4\text{V}_3\text{O}_{10}$. VESTA²³ was used for bond valence sum analysis of vanadium oxidation states, for crystal structure images, and for magnetic space group images. Bond valence sum parameters came from analysis by Brown and Altermatt²⁴ and by Liu and Thorp,²⁵ and the B parameter was set at 0.37 Å based on their analysis. For all BVS calculations, nickel and oxygen had fixed oxidation states of +2 and -2, respectively.

Magnetic property measurements were performed with powder mounted in a brass sample holder in a Quantum Design Magnetic Property Measurement System (MPMS3) vibrating sample magnetometer. For heat capacity measurements, collected using a Quantum Design Physical Property Measurement System (PPMS), powder was dry pressed and mounted with Apiezon N-grease. Energy dis-

persive X-ray fluorescence spectrometry (XRF) was performed on sample powders with a Shimadzu EDX-7000 spectrometer. A Kratos Axis Ultra, calibrated with Cu 2p_{3/2} and Au 4f_{7/2} standards, was used for X-ray photoelectron spectroscopy (XPS). Binding energy referencing was made to the C 1s peak (285.0 eV). A Cary 5000 spectrophotometer was used for UV-vis diffuse reflectance data.

A JEOL 6060LV scanning electron microscope equipped with an IXRF EDS Elemental Analysis System was used for micrographs and energy dispersive spectroscopy (EDS). A grain of $\text{Ni}_4\text{V}_3\text{O}_{10}$ was isolated within a sintered pellet using electron backscatter diffraction (EBSD) with a Thermo Scientific Scios2 Dual-Beam SEM/FIB and was cut from the bulk sample in an FEI Helios 600i Dual Beam SEM/FIB. Electron energy loss spectroscopy (STEM-EELS) was performed on the grain with an FEI Themis Z Advanced Probe Aberration Corrected Analytical TEM/STEM.

Computational Procedure

First-principles simulations were performed using spin polarized density-functional theory (DFT)²⁶ as implemented in the Vienna *Ab-initio* Simulation Package (VASP).^{27–29} To describe the exchange-correlation energy, the generalized-gradient approximation (GGA) developed by Perdew, Burke, and Ernzerhof (PBE)³⁰ was used, and to account for electron correlations, the Hubbard U method³¹ was applied. Similar to previous studies of other phases of the Ni–V–O system such as NiV_3O_8 , $\text{Ni}_3\text{V}_2\text{O}_8$, $\text{Ni}_2\text{V}_2\text{O}_7$, and NiVO_3 ,³² the simplified rotationally invariant $U - J$ on-site Coulomb interaction scheme developed by Dudarev *et al.*³³ was used with values of 6.2 eV for Ni d states and 3.2 eV for V d states. The projector-augmented wave (PAW) scheme³⁴ was used to describe the electron-ion interaction. Based on the results of a convergence test, the single-particle wave functions were expanded into a plane-wave basis up to a cutoff energy of 600 eV, and the Brillouin zone was sampled by a Γ -centered $9 \times 8 \times 8$ k-point mesh, al-

lowing for the computation of total energies converged to within 1.65 meV/atom.

The aforementioned occupational Ni/V site disorder of the $\text{Ni}_4\text{V}_3\text{O}_{10}$ phase is challenging to model computationally because the periodic boundary conditions cannot be imposed in the same way as in perfect crystals. To simulate this material, the unit cell derived from the powder X-ray diffraction experiments as shown in Fig. 2 was the starting point. As listed in Table 1, two sites, Ni1/V1 and Ni2/V2, have site disorder with Ni as the sites' primary element. Based on Ni:V occupancy ratios of about 0.8:0.2 and 0.7:0.3 for Ni1/V1 and Ni2/V2 sites, respectively, and taking into account that the Ni1/V1 site includes 8 atoms while the Ni2/V2 site hosts 2 atoms, all possible configurations in which 8 of these doubly occupied sites are filled with Ni and 2 of them are filled with V were found. This is a simple combinatorial problem leading to $\binom{10}{2} = 45$ configurations, which reduce to 8 symmetrically distinct classes (see Table S1³⁵). For all of these, band structures, projected electronic densities of states, and dielectric functions²⁹ were computed and are discussed below.

Results and Discussion

Composition

The crowded compositional space in which $\text{Ni}_4\text{V}_3\text{O}_{10}$ sits makes it difficult to isolate the phase. In an effort to optimize the synthesis temperature, ball-milled samples were fired under vacuum at 700°C, 800°C, 850°C, 950°C, and 1050°C. At 700°C, $\text{V}_{2-x}\text{Ni}_x\text{O}_3$ (45.2 wt%), $\text{Ni}_3\text{V}_2\text{O}_8$ (33.6 wt%), and NiO (19.7 wt%) impurities dominated, and little $\text{Ni}_4\text{V}_3\text{O}_{10}$ (1.5 wt%) was formed. At and above 850°C, $\text{Ni}_4\text{V}_3\text{O}_{10}$ was formed with NiO and $\text{V}_{2-x}\text{Ni}_x\text{O}_3$ impurities that increased with temperature, but without $\text{Ni}_3\text{V}_2\text{O}_8$. Firing at 800°C under vacuum consistently provided the highest purity samples. When fired in air at 800°C instead of under vacuum, vanadium was fully oxidized to V^{5+} , and $\text{Ni}_3\text{V}_2\text{O}_8$ was formed exclusively. Un-

der Ar flow, only 5.7 wt% of the product was $\text{Ni}_4\text{V}_3\text{O}_{10}$ (39.0 wt% $\text{Ni}_3\text{V}_2\text{O}_8$, 33.5 wt% $\text{V}_{2-x}\text{Ni}_x\text{O}_3$, 21.8 wt% NiO). Although NiVO_3 is closer on the phase diagram to $\text{Ni}_4\text{V}_3\text{O}_{10}$ than $\text{V}_{2-x}\text{Ni}_x\text{O}_3$, it was not observed under any of these synthesis conditions. In the past, NiVO_3 has been produced only by high pressure solid-state³⁶ and high pressure hydrothermal¹³ techniques.

According to Rietveld refinements of the X-ray diffraction data, the highest purity sample contained 89.5 ± 0.3 wt% $\text{Ni}_4\text{V}_3\text{O}_{10}$ for the ball milling technique and 86.8 ± 0.1 wt% $\text{Ni}_4\text{V}_3\text{O}_{10}$ for the hand grinding technique. Neutron powder diffraction data revealed that ball milling introduced an Fe_2O_3 impurity of about 0.03 wt% in the product. A small peak for this impurity could also be found in the 11-BM X-ray diffraction pattern at $d = 2.50$ Å (Fig. S1³⁵). The other expected prominent structural peaks of Fe_2O_3 at $d = 2.69$ and 3.67 Å overlap with peaks of other phases and thus were not distinguishable in the data. Qualitative XRF confirmed that Fe was present in ball-milled samples but absent in hand-ground samples.

With co-refinement of 11-BM X-ray diffraction and POWGEN neutron diffraction data for a sample, the composition of the new ternary phase was refined to $\text{Ni}_{3.9945}\text{V}_{3.0055}\text{O}_{10}$ (Ni and V $esd = \pm 0.0022$). The co-refinement presented no evidence of oxygen vacancies. It is assumed here that the composition is $\text{Ni}_4\text{V}_3\text{O}_{10}$. EDS point measurements corroborating this Ni:V ratio are presented in the Supporting Information.³⁵

Crystal Structure

The crystal structure of $\text{Ni}_4\text{V}_3\text{O}_{10}$ was solved in the $P4/n$ space group with powder X-ray diffraction data from a sample made by the ball milling procedure. The unit cell of $\text{Ni}_4\text{V}_3\text{O}_{10}$ contains two formula units and is shown in Fig. 2. The structure includes octahedral, tetrahedral, and square pyramidal cation-oxygen coordination geometries. While nickel ions are present only on octahedral sites, the vanadium ions occupy every cation

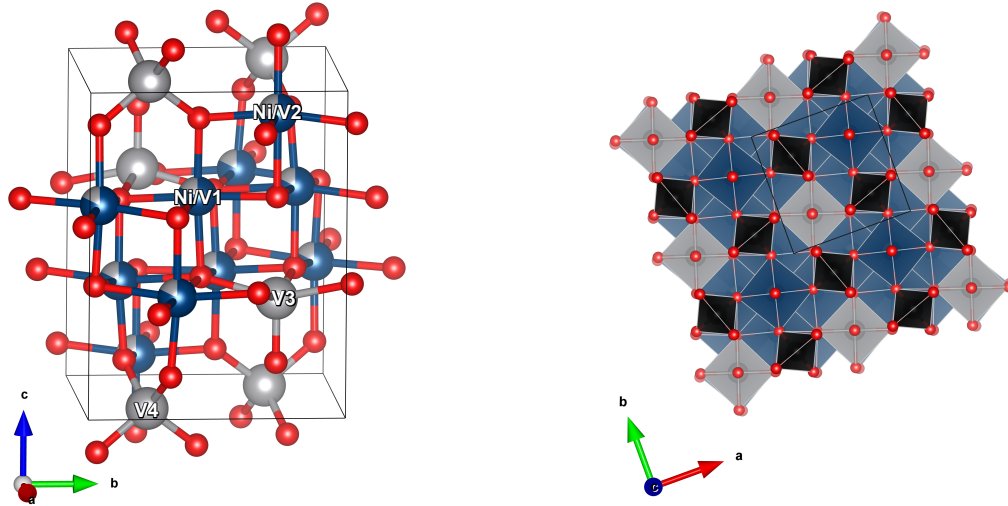


Figure 2: (Left) Unit cell of $\text{Ni}_4\text{V}_3\text{O}_{10}$. Ni ions are pictured in blue, V in gray, and O in red. The structure contains three metal-oxygen coordination geometries: octahedra, tetrahedra, and square pyramids. (Right) $2 \times 2 \times 1$ supercell of $\text{Ni}_4\text{V}_3\text{O}_{10}$ viewed down the c -axis. Ni/V ions in octahedra are colored blue. V ions in square pyramids are gray. V ions in tetrahedra are black. O ions are red.

site. The polyhedra form a set of three distorted planes normal to the c -axis and the structure contains a checkerboard pattern resembling a rock-salt structure.

The subsequent co-refinement to X-ray and neutron powder diffraction data included the new phase (87.4 wt%), $\text{V}_{2-x}\text{Ni}_x\text{O}_3$ (6.8 wt%), and NiO (5.8 wt%). The x value in $\text{V}_{2-x}\text{Ni}_x\text{O}_3$ refined to 0.5058 ± 0.0060 , indicating the solid solution was below its reported solubility limit of $x = 0.75$.¹⁶ The refinements and impurity phase contributions are shown in Fig. 3 and refined atomic parameters are reported in Table 1. The Fe_2O_3 impurity introduced by ball milling was not included due to its extremely small contribution to the structural peaks. Every peak reported by Gianoglio and Ramonda¹⁸ was observed.

Two cation sites are occupationally disordered with Ni as the sites' primary element. These cation sites form distorted rock-salt-like edge sharing octahedra with oxygen. NiVO_3 , NiV_3O_8 , and $\text{V}_{2-x}\text{Ni}_x\text{O}_3$ also contain metal-oxygen octahedra but no other coordination geometries. Of these, only $\text{V}_{2-x}\text{Ni}_x\text{O}_3$ involves occupational site disorder.

The other two metal sites in $\text{Ni}_4\text{V}_3\text{O}_{10}$ are occupied exclusively by vanadium. One, V3,

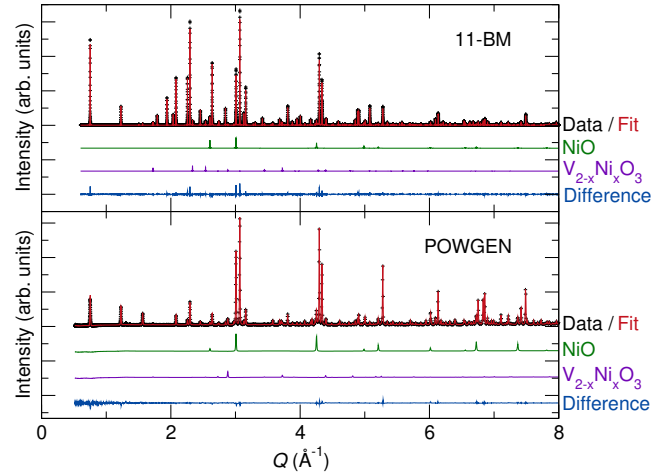


Figure 3: Rietveld co-refinement of synchrotron radiation powder X-ray diffraction (APS 11-BM) and time-of-flight powder neutron diffraction (ORNL POWGEN) data for a sample with 87.4 wt% $\text{Ni}_4\text{V}_3\text{O}_{10}$.

Table 1: Atomic data for $\text{Ni}_4\text{V}_3\text{O}_{10}$ (refined to $\text{Ni}_{3.9945}\text{V}_{3.0055}\text{O}_{10}$) from co-refinement of 300 K POWGEN powder neutron diffraction data and 11-BM powder X-ray diffraction data. $a = b = 6.478314(8)$ Å, $c = 8.352240(10)$ Å, space group $P4/n$.

Atom	Site	x	y	z	U_{iso} (Å ²)	Occupancy
Ni1/V1	8g	0.55160(5)	0.15332(5)	0.36493(3)	0.00311(4)	0.8219/0.1781(10)
Ni2/V2	2c	0.25	0.25	0.09935(8)	0.00522(14)	0.7069/0.2931(20)
V3	2c	0.25	0.25	0.66593(11)	0.00398(21)	1
V4	2a	0.25	0.75	0	0.00327(18)	1
O1	8g	0.03551(10)	0.65569(9)	0.38899(5)	0.00502(9)	1
O2	8g	0.54980(7)	0.17701(10)	0.12310(7)	0.00622(10)	1
O3	2c	0.25	0.25	0.35522(16)	0.00592(20)	1
O4	2c	0.25	0.25	0.86136(16)	0.00884(24)	1

has a square pyramidal arrangement where the square base is edge sharing and the top oxygen is corner sharing with the Ni/V octahedra. The square pyramidal coordination in $\text{Ni}_4\text{V}_3\text{O}_{10}$ makes it unique among the Ni–V–O phases plotted in Fig. 1. The second purely vanadium site, V4, is tetrahedrally coordinated to oxygen and is corner sharing with four octahedra.

Vanadium Oxidation States

The coordination environments of the vanadium cations appear tied to their oxidation states. Bond valence sum (BVS) analysis indicates that the tetrahedrally coordinated vanadium ions (V4) have a +5 oxidation state. Similarly, V^{5+} cations in $\text{Ni}_2\text{V}_2\text{O}_7$, $\text{Ni}_3\text{V}_2\text{O}_8$, and NiV_2O_6 exclusively form vanadium-oxygen tetrahedra. According to a statistical analysis of experimentally realized oxides by Waroquiers *et al.*, tetrahedral coordination for V^{5+} is the most likely geometry (67.27%).³⁷ The presence of V^{5+} on this site would necessitate V^{3+} within the material for charge balance because of the tight restriction on the composition seen in the diffraction co-refinement result. And the presence of V^{3+} cations is evidenced by BVS analysis of the square pyramidal vanadium sites (V3), where a mixed +3/+4 oxidation state is likely. Waroquiers *et al.* present square pyramidal coordination geometries as the second most likely for V^{4+} (13.35%) behind octahedral ones (71.08%). For V^{3+} , they show that octahedra are by far

the most likely (96.72%) whereas square pyramids are quite unlikely (0.01%).³⁷ This suggests that V^{4+} is more common on the V3 site and promotes the square pyramidal geometry derived from X-ray and neutron diffraction co-refinement while V^{3+} cations also occupying the site distort the polyhedron between geometries with octahedral and square pyramidal character.

BVS analysis of mixed occupancy sites can prove difficult, but Bosi demonstrates a technique where, in this case, BVS values obtained assuming a purely nickel or vanadium site are averaged while weighting by site occupancy.³⁸ Using Bosi’s procedure with the two Ni/V sites produces a predicted oxidation state of +3 for V1 and +4 for V2, more evidence for three vanadium oxidation states. If the V1, V2, and V4 sites contain only one vanadium oxidation state, as seems likely based on the BVS analysis, then in order to have charge balance, V3 would require an average oxidation state of +3.726. This seems plausible based on a +3/+4 weighted average using Bosi’s method. It also supports the square pyramidal arrangement of the site in the average crystallographic cell since more V^{4+} is present. It should be noted, however, that Bosi’s analysis assumes the structure contains unstrained polyhedra, and although it provides a better BVS fit for V3 than a purely +3 or +4 state BVS calculation, there is enough error to cast doubt on this approximation in this case, and other options need to be considered. BVS results for this method are summarized in Ta-

ble 2.

If instead one assumes that every vanadium ion has an oxidation state of +4, the average expected from the nominal chemical formula, the results produce significantly higher difference values for the Ni1/V1 (-0.173), V3 (-0.269), and V4 (+0.739) sites, where the difference is the nominal state minus the bond valence sum. Alternatively, if one believes that the average state of +4 is achieved with only two oxidation states, that would require an even mix of V^{3+} and V^{5+} because of how strongly the neutron and X-ray diffraction co-refinement restricts the stoichiometry. Optimizing BVS results in this case requires more inspection. The best fits for V1 and V4 are 100% V^{3+} and 100% V^{5+} , respectively, as in the three state case. The +3/+5 fractions for V2 and V3 then must be optimized under the restriction of charge balance for the system. This optimization results in a V2 +3/+5 fractional composition of 0.6545/0.3455 and a difference of 1×10^{-5} for Ni2/V2. This is an excellent fit, but the corresponding V3 composition of 0.5926 V^{3+} /0.4074 V^{5+} results in a difference of -0.249, almost twice the difference in the three oxidation state case. When requiring charge balance, there is no mixture of states for V2 and V3 that improves the results for both sites over the three state model. Therefore, since the three state case already describes V2 well and produces a significantly superior V3 fit, it is accepted here as the better description.

One final option to consider with BVS is to avoid occupancy weighted methods. If one instead proposes that V3 is exclusively +4 and that V4 is exclusively +5 (their closest fits for traditional, single state site BVS analysis), then a +3 oxidation state is required for V1 and V2 to achieve charge balance. The differences with this procedure are -0.294 for V3 and +0.078 for V4 and cannot be calculated for the mixed Ni/V sites. Therefore, this option still includes three oxidation states while increasing the difference for the V3 ion. It, as a result, offers no descriptive advantage, and the original three state case is accepted as the superior model.

XPS spectra for a $Ni_4V_3O_{10}$ sample and the V_2O_5 powder used for synthesis are shown in Fig. 4. Even after binding energy referencing to the C 1s peak, the V_2O_5 O 1s peak is +0.53 eV from its expected position at 530.0 eV, and the V $2p_{3/2}$ peak is +0.51 eV from its expected 517.2 eV.^{40,41} This consistent shift, though, does not prevent the analysis of vanadium oxidation states since it has been shown that despite shifts in O 1s position, the energy difference between the O 1s and V $2p_{3/2}$ peaks is a reliable measure of oxidation state.⁴² Expected shifts of binary vanadium oxides are ~ 12.80 eV for V_2O_5 , ~ 13.45 eV for VO_2 , and ~ 14.50 eV for V_2O_3 .⁴⁰ For the V_2O_5 reference, this difference is 12.82 eV; for $Ni_4V_3O_{10}$ it is 13.42 eV. Along with the expected increase in V $2p_{3/2}$ peak width from V^{5+} to V^{4+} ,⁴² this peak position difference for $Ni_4V_3O_{10}$ indicates the presence of V^{4+} .

The presence of an additional shoulder in the O 1s peak of $Ni_4V_3O_{10}$ also reveals moisture contamination on the surface. This effect has been noted in samples of V_2O_5 ,⁴¹ vanadium-yttrium hydrates,⁴³ and NiO.⁴⁴ This oxide/hydroxide layer likely protects vanadium near the surface of $Ni_4V_3O_{10}$ from oxidizing to V^{5+} in air. This data, though, cannot reveal the presence of multiple oxidation states within the bulk of the material.

To try to probe the bulk, a STEM-EELS spectrum was collected for a $Ni_4V_3O_{10}$ grain oriented down the [001] direction but did not provide additional insights into the oxidation states of $Ni_4V_3O_{10}$ (see Supporting Information³⁵). Consequently, assignment of three vanadium oxidation states to the different vanadium sites is made on the necessity from bond valence analysis to accommodate tetrahedral V^{5+} and an average V^{4+} valence for charge neutrality and is further supported by the broad V $2p_{3/2}$ XPS peak.

Although oxides containing cations exhibiting three oxidation states are rare, with only nine others reported, they have similarities to $Ni_4V_3O_{10}$. The multiple state cations in most cases occupy multiple coordination environments in the structures^{45–53} with the

Table 2: Best bond valence sum analysis fits for $\text{Ni}_4\text{V}_3\text{O}_{10}$ when following techniques for mixed sites proposed by Bosi.³⁸

Site	Oxygen Coordination	Nominal V Valence	Weighted Site Valence	R_0	BVS	Difference
Ni1/V1	Octahedral	+3	+2.175	1.67 ^a (Ni^{2+}), 1.743 ^b (V^{3+})	2.126	-0.049
Ni2/V2	Octahedral	+4	+2.572	1.67 ^a (Ni^{2+}), 1.784 ^b (V^{4+})	2.529	-0.043
V3	Square Pyramidal	+3/+4	+3.726*	1.743 ^b (V^{3+}), 1.784 ^b (V^{4+})	3.600	-0.126
V4	Tetrahedral	+5	+5	1.803 ^b (V^{5+})	5.078	+0.078

^a (W. Liu and H.H. Thorp, 1993)²⁵

^b (I.D. Brown and D. Altermatt, 1985)³⁹

* Valence required for charge neutrality if the other metal sites have a single V valence state

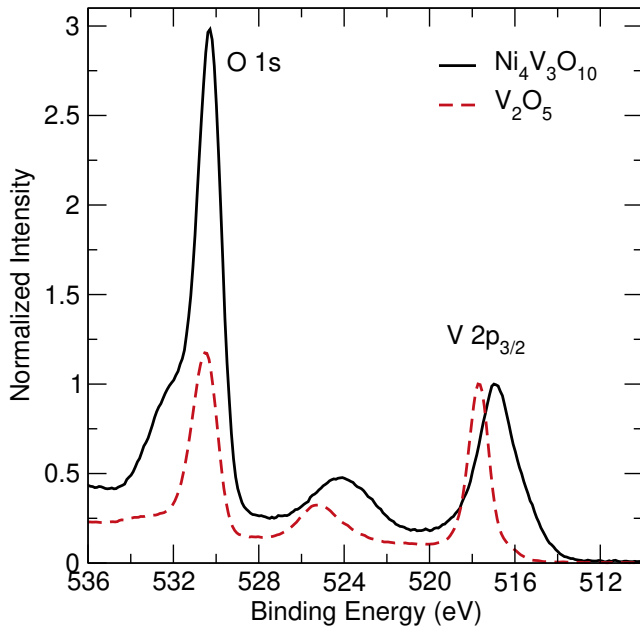


Figure 4: XPS spectra of the O 1s and V $2p_{3/2}$ peaks for $\text{Ni}_4\text{V}_3\text{O}_{10}$ and V_2O_5 (99.6%, as received). The $\text{Ni}_4\text{V}_3\text{O}_{10}$ spectrum indicates the presence of V^{4+} as well as an oxide/hydroxide surface layer.

only exception being Mn in the perovskite $(\text{La,Ca,K})\text{MnO}_3$.^{54,55} Notably, $\text{Ba}_{15}\text{V}_{12}\text{S}_{34}\text{O}_3$ contains V^{3+} on octahedral sites, V^{4+} on a site distorted between square pyramidal (“V1a”) and octahedral (“V1b”) coordination, and V^{5+} on a tetrahedral site.⁵³ These coordination structures match the behavior of $\text{Ni}_4\text{V}_3\text{O}_{10}$ well. Also deserving special attention are $\text{Ni}_x\text{Mn}_{3-x}\text{O}_4$ ⁴⁷ and $\text{Cu}_x\text{Mn}_{3-x}\text{O}_4$,⁴⁸ two occupationally disordered spinels, a structure type containing octahedral and tetrahedral coordination geometries. In both, the tetrahedral sites are Mn^{2+} , and the octahedral sites are mixed $\text{Mn}^{3+/4+}$. In the same way, $\text{H}_x\text{Li}_y\text{Co}_{3-\delta}\text{O}_4$ (typically near $\text{H}_{0.37}\text{Li}_{0.16}\text{Co}_{2.66}\text{O}_4$) forms a spinel structure with Co^{2+} in the tetrahedral sites and with Co^{3+} and Co^{4+} on the octahedral sites. Li substitution into the base Co_3O_4 structure promotes the presence of Co^{4+} .^{49,56–58} These three compounds demonstrate how occupational disorder can promote the coexistence of three cation oxidation states.

Absorption Properties and Band Character

UV-Vis spectroscopy reflectance data was transformed using the Kubelka-Munk theory⁵⁹ to give the absorption spectrum of $\text{Ni}_4\text{V}_3\text{O}_{10}$. A Tauc plot for modelling direct band gaps⁶⁰ was then constructed to observe the gap (Fig. 5).

Following the procedure of Makula *et al.*, the intersection of regression lines was used to determine the band gap associated with an onset in the Tauc plot.⁶¹ Two onsets were observed, one at 0.79 eV and another at 1.29 eV.

Absorption coefficients computed using DFT+*U* for the 8 permutations of Ni/V ordered classes are shown in Fig. 6. Classes A and B show a peak structure in the <4 eV energy region while classes C-H show steps in this energy range. While classes A and B have a non-zero absorption coefficient at energy values less than 1 eV, the others do not until around 1.5 eV. The densities of states for each class (see Supporting Information³⁵) reveal that the differences in classes A and B arise from an additional V d orbital in the valence band. This additional orbital would be consistent with inclusion of V³⁺ 3*d*² states that are necessary to balance the V⁵⁺ that is clearly evident in bond valence analysis. This difference also manifests itself in the calculated band gaps in Table 3, where the “Gap 1” values (associated with spin component 1) are significantly smaller for classes A and B. Band structure plots are also available in the Supporting Information.³⁵

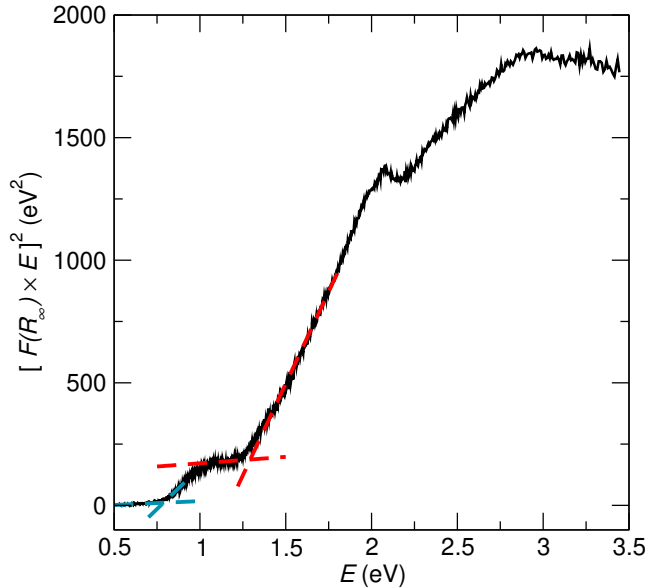


Figure 5: Tauc plot showing intersecting dashed lines at the onsets associated with direct band gaps.

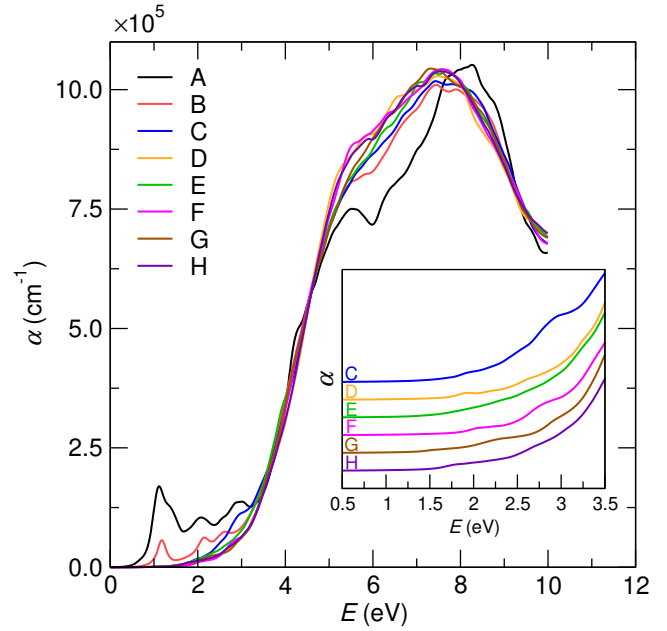


Figure 6: Calculated absorption coefficients, α , for the 8 classes. Classes A and B show a noticeable peak structure in the <4 eV region. The inset shows the more featureless shape of the other 6 classes at low energy with the values of α offset uniformly for each.

Magnetic Properties

Magnetometry Data

The magnetic properties of Ni₄V₃O₁₀ were explored with a sample produced by the hand grinding method to eliminate the contribution of any Fe₂O₃ impurity. The field cooled (FC) and zero field cooled (ZFC) magnetization curves were measured between 2 and 400 K and are shown in Fig. 7. The most frequent impurity in Ni₄V₃O₁₀ samples, V_{2-x}Ni_xO₃, is a ferromagnet with an unreported magnetic structure. It has a Curie temperature of 142 K and an additional transition, here denoted T^* , at 56 K. The FC curve for this impurity is shown in Fig. S7.³⁵ Since a sharp increase in magnetization at T_C occurs in any sample with a V_{2-x}Ni_xO₃ impurity, we can be sure that the magnetization data in Figure 7 is from Ni₄V₃O₁₀ alone. The bifurcation of the FC and ZFC curves in Fig. 7 indicates a Néel temperature $T_N = 38$ K.

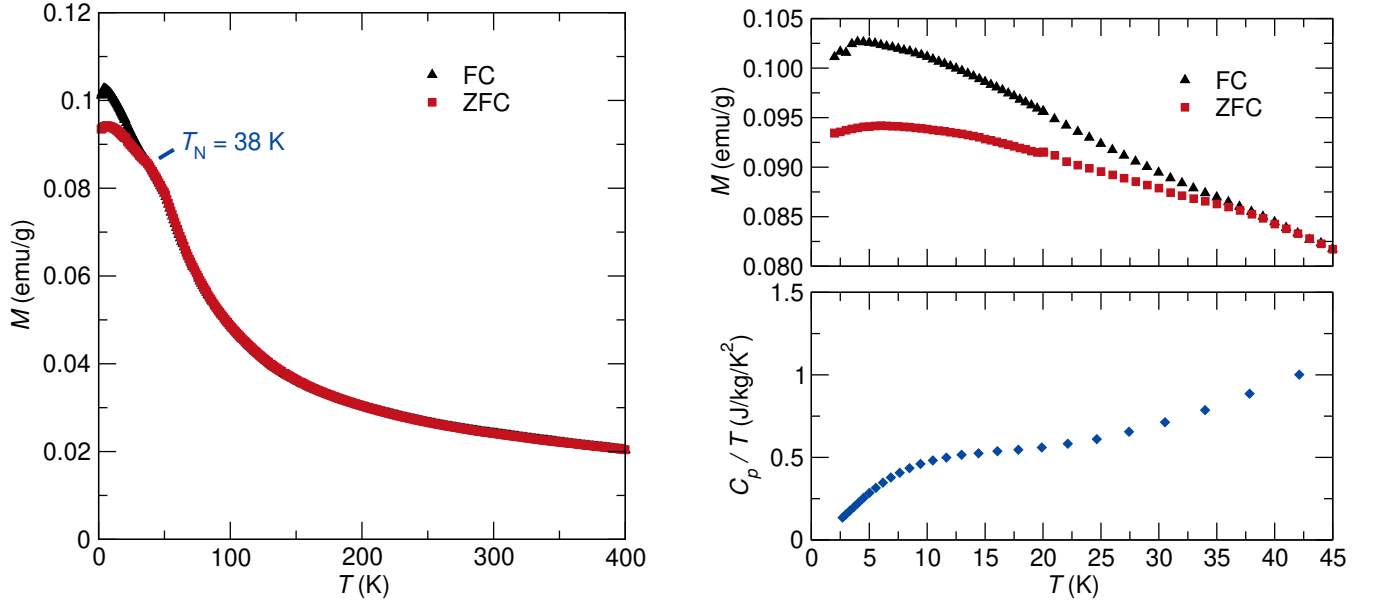


Figure 7: (Left) Field cooling and zero field cooling magnetization collected from 2–400 K at 1000 Oe for a $\text{Ni}_4\text{V}_3\text{O}_{10}$ sample. The Néel temperature for $\text{Ni}_4\text{V}_3\text{O}_{10}$ manifests as the split between the curves at 38 K. (Right) Low temperature FC and ZFC data paired with the temperature normalized heat capacity of $\text{Ni}_4\text{V}_3\text{O}_{10}$ from 2–45 K. The broad hump centered below T_N in the heat capacity data has been noted in other materials with magnetic frustration,^{62,63} site disorder,⁶⁴ and complex coordination and oxidation chemistry.⁵³

Table 3: Calculated band gaps for the 8 classes along with their relative calculated energies. Gap 1 (2) corresponds to the smallest band gap for spin component 1 (2).

Class	Gap 1 (eV)	Gap 2 (eV)	Relative Total Energy (meV/atom)
A	0.54	3.21	+45.7
B	0.68	3.00	+25.6
C	1.33	2.92	± 0
D	1.76	3.36	+5.07
E	1.31	2.95	+51.5
F	1.90	3.12	+38.5
G	1.42	2.82	+12.0
H	1.54	3.09	+7.64

Neutron Diffraction Data

In addition to magnetometry data, POWGEN neutron powder diffraction data collected while cooling from 80 K to around 9 K confirms this transition. A significant magnetic peak that appears at $d = 5.57$ Å indicates that the transition at 38 K corresponds to $\text{Ni}_4\text{V}_3\text{O}_{10}$. The onset of this peak can be observed using a contour plot con-

structed with 5 K diffraction data bins (Fig. 8). Its intensity relative to the background is plotted in Fig. S8.³⁵ Additional low intensity peaks are apparent in the long isothermal neutron powder diffraction collection at 6.4 K at $d = 10.40, 10.06, 5.57, 5.39, 3.97, 2.88,$ and 2.36 Å. These peaks are tentatively assigned to $\text{Ni}_4\text{V}_3\text{O}_{10}$ and are plotted in Fig. 9.

By exploring the maximal magnetic space groups for the $P4/n$ crystallographic space group, it is clear that the magnetic structure of $\text{Ni}_4\text{V}_3\text{O}_{10}$ is not a simple commensurate phase with a magnetic propagation vector of $\mathbf{k} = \mathbf{0}$. There are six maximal space groups: $P4/n$ and $P2'/c'$ can be ruled out due to their ferromagnetic ordering, while $P4'/n$ and $P4'/n'$ do not allow local moments on the Ni2/V2 or V3 sites. To visualize the remaining two, magnetic moments with arbitrary and equal magnitudes are assigned to each space group based on the allowed moment directions. The first magnetic space group, $P4/n'$, allows for a , b , and c components of the moment on Ni1/V1 and for only a c component on Ni2/V2 and V3. The other, $P2'/c$, splits Ni1/V1 into

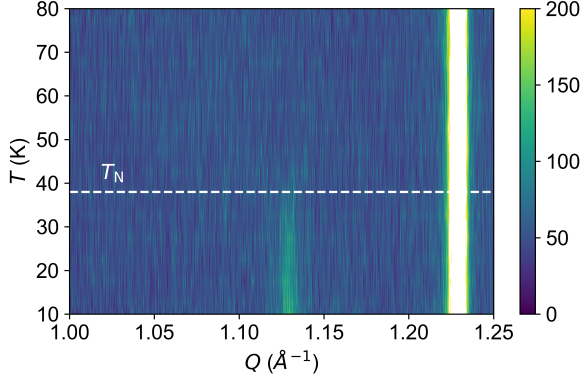


Figure 8: Contour plot using 5 K splits of ramping data. The new magnetic peak at $Q = 1.13 \text{ \AA}^{-1}$ ($d = 5.57 \text{ \AA}$) is shown along with the structural peak at $Q = 1.23 \text{ \AA}^{-1}$ ($d = 5.11 \text{ \AA}$). The scale used improves the visibility of the magnetic peak, but it also tops off the structural peak's max intensity of around 800 (arbitrary units). The magnetic peak clearly appears below T_N .

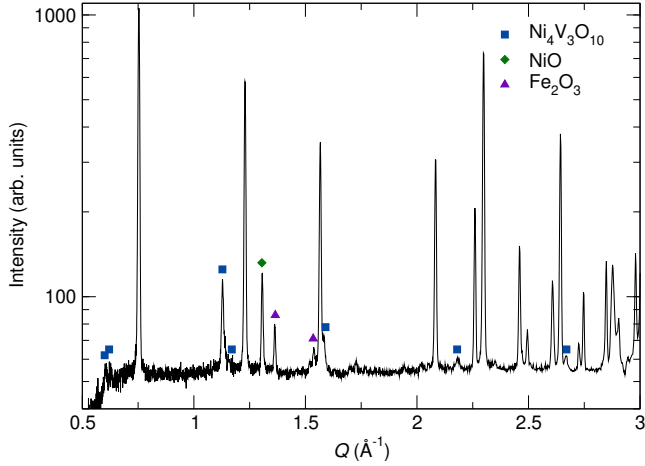


Figure 9: Peaks in the 6.4 K neutron powder diffraction data that are not present at room temperature are marked with squares. NiO and Fe_2O_3 impurity magnetic peaks that are present at 6.4 K and room temperature are marked as well. All unmarked peaks are structural.

two magnetic symmetry sites, each with a possible a , b , and c component to the magnetic moment, but unlike with $P4/n'$, Ni2/V2 and V3's magnetic moments are restricted to the ab -plane.

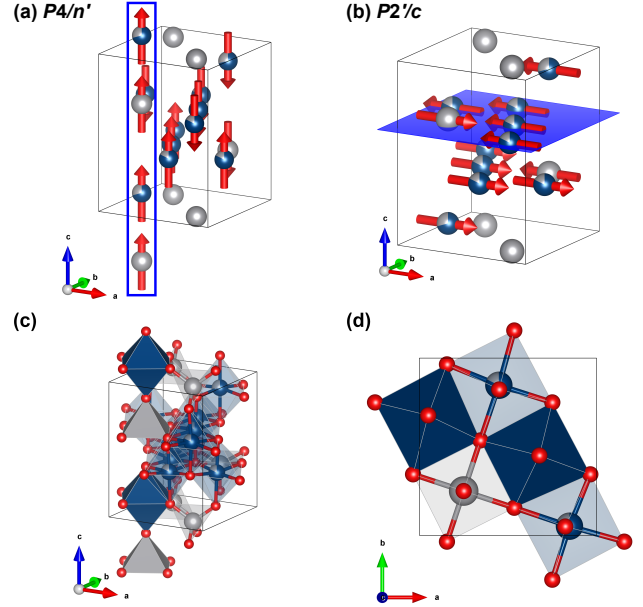


Figure 10: The two $\mathbf{k} = 0$ maximal magnetic space groups for $\text{Ni}_4\text{V}_3\text{O}_{10}$ with antiparallel moment arrangements on the Ni1/V1, Ni2/V2, and V3 sites. (a) shows a $P4/n'$ unit cell with a box enclosing the four inline ions that violate antiferromagnetic ordering. (b) shows a $P2'/c$ unit cell with a (001) plane. In (c), the Ni2/V2-O-V3 bonding path is presented with opaque polyhedra, and in (d), the Ni1/V1-O-Ni1/V1 path is presented with opaque polyhedra. These bonding structures paired with the ions' local moments violate antiferromagnetic ordering. Each space group contains both coordination violations.

However, antiferromagnetic ordering is violated for both $P4/n'$ and $P2'/c$ in $\text{Ni}_4\text{V}_3\text{O}_{10}$ through Ni2/V2-O-V3 bonding paths between cells along the c -axis and also through Ni1/V1-O-Ni1/V1 bonding paths within the crystallographic cell. Figure 10a shows the spin arrangement of $P4/n'$, and Fig. 10b shows that of $P2'/c$. Oxide ions are omitted for clarity of the spin orientations. Figure 10a includes an additional Ni2/V2 ion from the cell above and a V3 ion from the cell below. The polyhedral connections between these ions (opaque

polyhedra in Fig. 10c) demonstrate how these connections break antiferromagnetic ordering across 180° superexchange paths. Moreover, Fig. 10b includes a (001) slice in the cell to illustrate the other discrepancy's location. In this slice, the opaque polyhedra in Fig. 10d have the same spin orientations and violate antiferromagnetic ordering. Both $P4/n'$ and $P2'/c$ contain both spin orientation issues.

These arguments explain why $\mathbf{k} = \mathbf{0}$ ordering is not adopted in $\text{Ni}_4\text{V}_3\text{O}_{10}$. The magnetic peak assigned to $\text{Ni}_4\text{V}_3\text{O}_{10}$ at $d = 5.57 \text{ \AA}$ could be indexed as (003) under the assumption of c -axis doubling, resulting in a magnetic propagation vector $\mathbf{k} = (0, 0, \frac{1}{2})$, but this assumption also produces structures incompatible with antiferromagnetic ordering and does not index the remaining neutron diffraction peaks.

Frustrated Magnetism in $\text{Ni}_4\text{V}_3\text{O}_{10}$

Having established that $\text{Ni}_4\text{V}_3\text{O}_{10}$ has a Néel temperature at 38 K and does not experience $\mathbf{k} = \mathbf{0}$ ordering, it is worth further exploring its nontrivial magnetic properties. A Curie-Weiss fit to magnetometry data above 300 K, shown in Fig. 11, results in a Curie-Weiss parameter $\theta = -234 \text{ K}$. Combined with the information about T_N from the low temperature magnetometry and neutron diffraction data, this indicates frustrated antiferromagnetic ordering with a frustration index of 6.2.

Additionally, low temperature heat capacity measurements on $\text{Ni}_4\text{V}_3\text{O}_{10}$ show a broad peak below 30 K. As can be seen in Fig. 7, this does not correspond to a change in the magnetization curves. A similar heat capacity response has been noted in several spinel systems where mixed or frustrated magnetic behavior is present. For CoAl_2O_4 spinels, Tristan *et al.* show that with low substitution of Co onto the primarily Al octahedral site, a hump in the heat capacity appears slightly above the characteristic temperature, but with a greater degree of substitution, the hump broadens and appears at a lower temperature than the bifurcation in the FC and ZFC susceptibility curves.⁶³ They associate this behavior with a mixed magnetic phase. Ghara *et al.* likewise

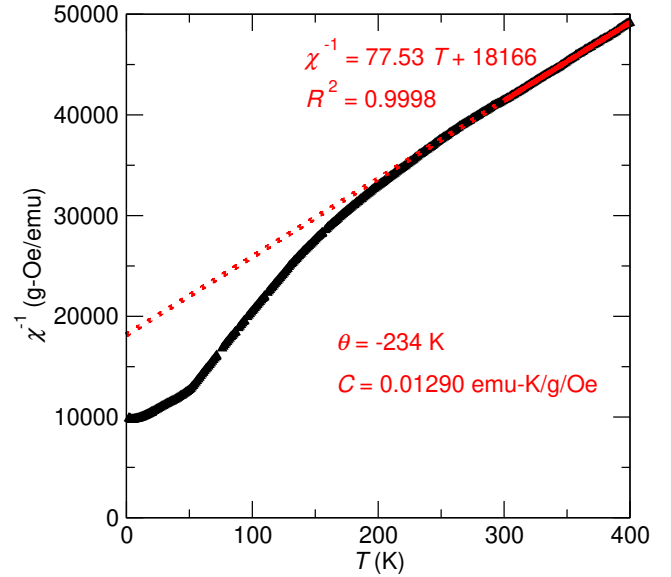


Figure 11: Curie-Weiss fit to 1000 Oe field cooling data above 300 K for $\text{Ni}_4\text{V}_3\text{O}_{10}$.

observe that increasing cation antisite disorder in CoAl_2O_4 samples shifts the heat capacity magnetic peak to lower temperatures and broadens it.⁶⁴ Another spinel system, FeSc_2S_4 , also shows a broad peak below its ordering temperature that is associated with geometric magnetic frustration⁶² and disorder in the sample.⁶⁵ $\text{Ba}_{15}\text{V}_{12}\text{S}_{34}\text{O}_3$, noted before for its structural similarities to $\text{Ni}_4\text{V}_3\text{O}_{10}$ and its inclusion of V^{3+} , V^{4+} , and V^{5+} cations, similarly exhibits antiferromagnetic interactions and a broad hump in its C_P/T curve below the bifurcation of the FC and ZFC curves.⁵³ Therefore, frustrated magnetic behavior in $\text{Ni}_4\text{V}_3\text{O}_{10}$ appears to lead to weak, incommensurate ordering that emerges over a range of temperatures below T_N . Single crystals may be needed to further explore the magnetic structure.

Conclusions

The crystal structure and antiferromagnetism of $\text{Ni}_{3.9945}\text{V}_{3.0055}\text{O}_{10}$ have been presented. Two methods of powder preparation were used to form the structure at 800°C . Although it requires much less time to achieve the same level of $\text{Ni}_4\text{V}_3\text{O}_{10}$ content, the ball milling method results in a small Fe_2O_3 impurity that can affect magnetic characterization. The ma-

terial is distinct from others in the Ni-V-O system in its inclusion of three metal-oxygen coordination structures, and the presence of three vanadium oxidation states, which is ambiguous by XPS or STEM-EELS but is supported by BVS analysis and neutron/X-ray co-refinement, would place it in a class of only nine other oxides. DFT+ U calculations for representatives of the 8 symmetrically distinct classes show varying absorption coefficient and band gap behavior due to the presence or absence of an additional $V^{3+} 3d^2$ orbital in the valence band. The structure's complexity, the emergence of low intensity magnetic peaks, and the presence of $V_{2-x}Ni_xO_3$, a ferromagnetic material with an unsolved magnetic structure, prevented the solution of the magnetic structure of $Ni_4V_3O_{10}$ from a powder sample, although $\mathbf{k} = \mathbf{0}$ and $\mathbf{k} = (0, 0, \frac{1}{2})$ magnetic structures were ruled out. Still, magnetometry, neutron powder diffraction data, and heat capacity measurements showed that $Ni_4V_3O_{10}$ is antiferromagnetic ($T_N = 38$ K) with strong geometric frustration arising from staggered rock-salt-like motifs. Further study into single crystal growth of the material could lead to the solution of the material's magnetic structure, could provide data for understanding the variability of the Ni/V site mixing, and could allow for a more precise determination of the vanadium oxidation state distribution.

Acknowledgement Synthesis and characterization were supported by the US Department of Energy (DOE), Basic Energy Sciences (grant No. DE-SC0013897) for Early Career Research and were carried out in part at the Materials Research Laboratory (MRL) Central Research Facilities, University of Illinois. The STEM experiments were likewise carried out at the MRL Central Research Facilities and were supported by the Air Force Office of Scientific Research under award FA9550-20-1-0302 and by the National Science Foundation under grant No. 1922758. Computational work was supported by Illinois MRSEC, NSF award No. DMR-1720633; this work made use of the Illinois Campus Cluster, a computing resource that is operated by the Illinois

Campus Cluster Program (ICCP) in conjunction with the National Center for Supercomputing Applications (NCSA) and which is supported by funds from the University of Illinois at Urbana-Champaign. Neutron scattering was performed at the Spallation Neutron Source, a DOE Office of Science User Facility operated by the Oak Ridge National Laboratory. Use of synchrotron X-ray powder diffraction at beamline 11-BM of the Advanced Photon Source at Argonne National Laboratory was supported by the U.S. Department of Energy, Office of Science, Office of Basic Energy Sciences, under Contract No. DE-AC02-06CH11357.

Supporting Information Available

The following Supporting Information is available free of charge at the ACS website:

Figure S1. Fe_2O_3 impurity peak in neutron diffraction data; Figure S2. SEM image of sample used for EDS point measurements; Table S1. DFT simulation cell configurations; Table S2. DFT+ U total energy results; Figure S3. DFT simulation cell; Figure S4. DFT+ U calculated band structures; Figure S5. DFT+ U projected densities of states; Figure S6. STEM-EELS spectrum for a grain of $Ni_4V_3O_{10}$; Figure S7. Field cooling magnetization curve of $V_{2-x}Ni_xO_3$; Figure S8. $Ni_4V_3O_{10}$ magnetic peak intensity relative to background intensity

References

- (1) He, Z.; Ueda, Y.; Itoh, M. Crystal growth of $Ni_3V_2O_8$ by flux method. *Journal of Crystal Growth* **2006**, *297*, 1–3.
- (2) Rogado, N.; Lawes, G.; Huse, D. A.; Ramirez, A.; Cava, R. J. The Kagomé staircase lattice: magnetic ordering in $Ni_3V_2O_8$ and $Co_3V_2O_8$. *Solid State Communications* **2002**, *124*, 229–233.
- (3) Hosseini, H.; Shahrokhian, S. Advanced binder-free electrode based on

- core-shell nanostructures of mesoporous $\text{Co}_3\text{V}_2\text{O}_8\text{-Ni}_3\text{V}_2\text{O}_8$ thin layers@porous carbon nanofibers for high-performance and flexible all-solid-state supercapacitors. *Chemical Engineering Journal* **2018**, *341*, 10–26.
- (4) Huang, Y.; Feng, X.; Li, C.; Li, Y.; Chen, X.; Gao, X.; Chen, C.; Guang, Z.; Liu, P. Construction of hydrangea-like $\text{ZnCo}_2\text{O}_4/\text{Ni}_3\text{V}_2\text{O}_8$ hierarchical nanostructures for asymmetric all-solid-state supercapacitors. *Ceramics International* **2019**, *45*, 15451–15457.
 - (5) Liu, X.; Wang, J.; Yang, G. In situ growth of the $\text{Ni}_3\text{V}_2\text{O}_8\text{@PANI}$ composite electrode for flexible and transparent symmetric supercapacitors. *ACS Applied Materials & Interfaces* **2018**, *10*, 20688–20695.
 - (6) Vishnukumar, P.; Saravanakumar, B.; Ravi, G.; Ganesh, V.; Guduru, R. K.; Yuvakkumar, R. Synthesis and characterization of $\text{NiO}/\text{Ni}_3\text{V}_2\text{O}_8$ nanocomposite for supercapacitor applications. *Materials Letters* **2018**, *219*, 114–118.
 - (7) Rozier, P.; Combes, M.; Galy, J. NiV_3O_8 single crystal structure determination and comparison with polymorphic forms of ZnV_3O_8 and MgV_3O_8 . *Journal of Physics and Chemistry of Solids* **2001**, *62*, 1401–1408.
 - (8) He, Z.; Yamaura, J.-I.; Ueda, Y.; Cheng, W. Crystal growth and multiple magnetic transitions of the spin-1 chain system $\text{Ni}_2\text{V}_2\text{O}_7$. *Physical Review B* **2009**, *79*, 092404.
 - (9) Ali, E. B.; Bernede, J.; Guyomard, D. $\text{Ni}_2\text{V}_2\text{O}_7$ thin films for negative electrode application of rechargeable microbatteries. *Thin Solid Films* **2002**, *402*, 215–221.
 - (10) Cui, P.; Liang, Y.; Zhan, D.; Zhao, Y. Synthesis and characterization of NiV_3O_8 powder as cathode material for lithium-ion batteries. *Electrochimica Acta* **2014**, *148*, 261–265.
 - (11) Ni, S.; Ma, J.; Lv, X.; Yang, X.; Zhang, L. The preparation of $\text{NiV}_3\text{O}_8/\text{Ni}$ composite via an *in situ* corrosion method and its use as a new sort of anode material for Li-ion batteries. *Journal of Materials Chemistry A* **2014**, *2*, 8995–8998.
 - (12) Ni, S.; Ma, J.; Zhang, J.; Yang, X.; Zhang, L. Excellent electrochemical performance of NiV_3O_8 /natural graphite anodes via novel *in situ* electrochemical reconstruction. *Chemical Communications* **2015**, *51*, 5880–5882.
 - (13) McNulty, D.; Collins, G.; O'Dwyer, C. NiVO_3 fused oxide nanoparticles—an electrochemically stable intercalation anode material for lithium ion batteries. *Journal of Materials Chemistry A* **2018**, *6*, 18103–18115.
 - (14) Zhou, Z.; Zhang, J.; Chen, S.; Yao, H.; Zhao, Y.; Kuang, Q.; Fan, Q.; Dong, Y. The electrochemical performance and multielectron reaction mechanism of NiV_2O_6 as a novel anode material for lithium-ion batteries. *Electrochimica Acta* **2020**, *359*, 136979.
 - (15) Li, Y.; Sun, H.; Yang, Y.; Cao, Y.; Zhou, W.; Chai, H. Controllable fabrication of NiV_2O_6 nanosphere as a high-performance flexible all-solid-state electrode material for supercapacitors. *Journal of Colloid and Interface Science* **2020**, *580*, 298–307.
 - (16) Bouloux, J.-C.; Milosevic, I.; Sénégas, J. Étude structurale et magnétique comparative des solutions solides $\text{M}_x^{2+}\text{V}_x^{4+}\text{V}_{2-2x}^{3+}\text{O}_3$ (M= Mg, Ni). *Revue de Chimie Minérale* **1974**, *11*, 701–709.
 - (17) Rozier, P.; Ratuszna, A.; Galy, J. Comparative Structural and Electrical Studies of V_2O_3 and $\text{V}_{2-x}\text{Ni}_x\text{O}_3$ ($0 < x < 0.75$)

- Solid Solution. *Zeitschrift für anorganische und allgemeine Chemie* **2002**, 628, 1236–1242.
- (18) Gianoglio, C.; Ramonda, G. Recherches sur le Système Nickel-Vanadium-Oxygène. *Rev. int. Htes Temp. et Réfract.* **1973**, 10, 27–30.
 - (19) Favre-Nicolin, V.; Černý, R. FOX, ‘free objects for crystallography’: a modular approach to ab initio structure determination from powder diffraction. *Journal of Applied Crystallography* **2002**, 35, 734–743.
 - (20) Toby, B. H.; Von Dreele, R. B. GSAS-II: the genesis of a modern open-source all purpose crystallography software package. *Journal of Applied Crystallography* **2013**, 46, 544–549.
 - (21) Capillas, C.; Tasci, E. S.; de la Flor, G.; Orobengoa, D.; Perez-Mato, J. M.; Aroyo, M. I. A new computer tool at the Bilbao Crystallographic Server to detect and characterize pseudosymmetry. *Zeitschrift für Kristallographie-Crystalline Materials* **2011**, 226, 186–196.
 - (22) Perez-Mato, J.; Gallego, S.; Tasci, E.; Elcoro, L.; de la Flor, G.; Aroyo, M. Symmetry-based computational tools for magnetic crystallography. *Annual Review of Materials Research* **2015**, 45, 217–248.
 - (23) Momma, K.; Izumi, F. VESTA 3 for three-dimensional visualization of crystal, volumetric and morphology data. *Journal of Applied Crystallography* **2011**, 44, 1272–1276.
 - (24) Brown, I.; Altermatt, D. Bond-valence parameters obtained from a systematic analysis of the inorganic crystal structure database. *Acta Crystallographica Section B* **1985**, 41, 244–247.
 - (25) Liu, W.; Thorp, H. H. Bond valence sum analysis of metal-ligand bond lengths in metalloenzymes and model complexes. 2. Refined distances and other enzymes. *Inorganic Chemistry* **1993**, 32, 4102–4105.
 - (26) Hohenberg, P.; Kohn, W. Inhomogeneous electron gas. *Physical review* **1964**, 136, B864.
 - (27) Kresse, G.; Furthmüller, J. Efficient iterative schemes for ab initio total-energy calculations using a plane-wave basis set. *Physical Review B* **1996**, 54, 11169.
 - (28) Kresse, G.; Joubert, D. From ultra-soft pseudopotentials to the projector augmented-wave method. *Physical Review B* **1999**, 59, 1758.
 - (29) Gajdoš, M.; Hummer, K.; Kresse, G.; Furthmüller, J.; Bechstedt, F. Linear optical properties in the projector-augmented wave methodology. *Physical Review B* **2006**, 73, 045112.
 - (30) Perdew, J. P.; Burke, K.; Ernzerhof, M. Generalized gradient approximation made simple. *Physical Review Letters* **1996**, 77, 3865.
 - (31) Rohrbach, A.; Hafner, J.; Kresse, G. Electronic correlation effects in transition-metal sulfides. *Journal of Physics: Condensed Matter* **2003**, 15, 979.
 - (32) Jain*, A.; Ong*, S.; Hautier, G.; Chen, W.; Richards, W.; Dacek, S.; Cholia, S.; Gunter, D.; Skinner, D.; Ceder, G.; Persson, K.; (*=equal contributions), The Materials Project: A materials genome approach to accelerating materials innovation. *APL Materials* **2013**, 1, (mp-1395638, mp-1296598, mp-1768665, mp-1752536).
 - (33) Dudarev, S.; Botton, G.; Savrasov, S.; Humphreys, C.; Sutton, A. Electron-energy-loss spectra and the structural stability of nickel oxide: An LSDA+U study. *Physical Review B* **1998**, 57, 1505.
 - (34) Blöchl, P. E. Projector augmented-wave method. *Physical Review B* **1994**, 50, 17953.

- (35) See Supporting Information.
- (36) Chamberland, B. A study on the NiVO_3 system. *Journal of Solid State Chemistry* **1970**, *2*, 521–524.
- (37) Waroquiers, D.; Gonze, X.; Rignanese, G.-M.; Welker-Nieuwoudt, C.; Rosowski, F.; Göbel, M.; Schenk, S.; Degelmann, P.; André, R.; Glaum, R.; Hautier, G. Statistical analysis of coordination environments in oxides. *Chemistry of Materials* **2017**, *29*, 8346–8360.
- (38) Bosi, F. Bond valence at mixed occupancy sites. I. Regular polyhedra. *Acta Crystallographica Section B* **2014**, *70*, 864–870.
- (39) Brown, I.; Shannon, R. Empirical bond-strength–bond-length curves for oxides. *Acta Crystallographica Section A* **1973**, *29*, 266–282.
- (40) Hryha, E.; Rutqvist, E.; Nyborg, L. Stoichiometric vanadium oxides studied by XPS. *Surface and Interface Analysis* **2012**, *44*, 1022–1025.
- (41) Silversmit, G.; Depla, D.; Poelman, H.; Marin, G. B.; De Gryse, R. Determination of the V2p XPS binding energies for different vanadium oxidation states (V^{5+} to V^{0+}). *Journal of Electron Spectroscopy and Related Phenomena* **2004**, *135*, 167–175.
- (42) Mendialdua, J.; Casanova, R.; Barbaux, Y. XPS studies of V_2O_5 , V_6O_{13} , VO_2 and V_2O_3 . *Journal of Electron Spectroscopy and Related Phenomena* **1995**, *71*, 249–261.
- (43) Bondarenka, V.; Grebinskij, S.; Kaciulis, S.; Mattogno, G.; Mickevicius, S.; Tvardauskas, H.; Volkov, V.; Zakharchova, G. XPS study of vanadium–yttrium hydrates. *Journal of Electron Spectroscopy and Related Phenomena* **2001**, *120*, 131–135.
- (44) Oswald, S.; Brückner, W. XPS depth profile analysis of non-stoichiometric NiO films. *Surface and Interface Analysis* **2004**, *36*, 17–22.
- (45) David, R.; Kabbour, H.; Bordet, P.; Pelloquin, D.; Leynaud, O.; Trentesaux, M.; Mentré, O. Triple $\text{Co}^{II,III,IV}$ charge ordering and spin states in modular cobaltites: a systematization through experimental and virtual compounds. *Journal of Materials Chemistry C* **2014**, *2*, 9457–9466.
- (46) Euzen, P.; Leone, P.; Mansot, J.; Bonneau, P.; Palvadeau, P.; Queignec, M. Synthesis and structural studies of manganese oxyhalides with a multisite framework: Part two: $\text{Mn}_{7.5}\text{O}_{10}\text{Br}_3$, a new lacunar oxybromide. *Materials Research Bulletin* **1992**, *27*, 1423–1430.
- (47) Gillot, B.; Kharroubi, M.; Metz, R.; Legros, R.; Rousset, A. Electrical properties and cationic distribution in cubic nickel manganite spinels $\text{Ni}_x\text{Mn}_{3-x}\text{O}_4$, $0.57 < x < 1$. *Solid State Ionics* **1991**, *44*, 275–280.
- (48) Gillot, B.; Legros, R.; Metz, R.; Rousset, A. Electrical conductivity of copper and nickel manganites in relation with the simultaneous presence of Mn^{3+} and Mn^{4+} ions on octahedral sites of the spinel structure. *Solid State Ionics* **1992**, *51*, 7–9.
- (49) Godillot, G.; Guerlou-Demourgues, L.; Taberna, P.-L.; Simon, P.; Delmas, C. Original conductive nano- Co_3O_4 investigated as electrode material for hybrid supercapacitors. *Electrochemical and Solid State Letters* **2011**, *14*, A139–A142.
- (50) Gueho, C.; Giaquinta, D.; Mansot, J.; Ebel, T.; Palvadeau, P. Structure and magnetism of $\text{La}_4\text{Mn}_5\text{Si}_4\text{O}_{22}$ and $\text{La}_4\text{V}_5\text{Si}_4\text{O}_{22}$: Two new rare-earth transition metal sorosilicates. *Chemistry of Materials* **1995**, *7*, 486–492.

- (51) Mansot, J.; Leone, P.; Euzen, P.; Palvadeau, P. Valence of manganese, in a new oxybromide compound, determined by means of electron energy loss spectroscopy. *Microscopy Microanalysis Microstructures* **1994**, *5*, 79–90.
- (52) Nemrava, S.; Vinnik, D. A.; Hu, Z.; Valldor, M.; Kuo, C.-Y.; Zherebtsov, D. A.; Gudkova, S. A.; Chen, C.-T.; Tjeng, L. H.; Niewa, R. Three Oxidation States of Manganese in the Barium Hexaferite $\text{BaFe}_{12-x}\text{Mn}_x\text{O}_{19}$. *Inorganic Chemistry* **2017**, *56*, 3861–3866.
- (53) Wong, C. J.; Hopkins, E. J.; Prots, Y.; Hu, Z.; Kuo, C.-Y.; Pi, T.-W.; Valldor, M. Anionic ordering in $\text{Ba}_{15}\text{V}_{12}\text{S}_{34}\text{O}_3$, Affording three oxidation states of vanadium and a quasi-one-dimensional magnetic lattice. *Chemistry of Materials* **2016**, *28*, 1621–1624.
- (54) Feng, S.; Yuan, H.; Shi, Z.; Chen, Y.; Wang, Y.; Huang, K.; Hou, C.; Li, J.; Pang, G.; Hou, Y. Three oxidation states and atomic-scale p–n junctions in manganese perovskite oxide from hydrothermal systems. *Journal of Materials Science* **2008**, *43*, 2131–2137.
- (55) Li, M.; Huang, K.-K.; Chu, X.-F.; Du, Y.-Y.; Ge, L.; Sun, Y.; Hou, C.-M.; Feng, S.-H. Preparation of perovskite manganites with three oxidation states via the molten hydroxide method. *Chemical Journal of Chinese Universities* **2013**, *34*, 284–287.
- (56) Shaju, K.; Guerlou-Demourgues, L.; Godillot, G.; Weill, F.; Delmas, C. Strategies for synthesizing conductive spinel cobalt oxide nanoparticles for energy storage applications. *Journal of The Electrochemical Society* **2012**, *159*, A1934.
- (57) Godillot, G.; Huo, H.; Ménétrier, M.; Bourgeois, L.; Guerlou-Demourgues, L.; Delmas, C. Promising nanometric spinel cobalt oxides for electrochemical energy storage: investigation of Li and H environments by NMR. *The Journal of Physical Chemistry C* **2012**, *116*, 26598–26607.
- (58) Godillot, G.; Guerlou-Demourgues, L.; Croguennec, L.; Shaju, K.; Delmas, C. Effect of temperature on structure and electronic properties of nanometric spinel-type cobalt oxides. *The Journal of Physical Chemistry C* **2013**, *117*, 9065–9075.
- (59) Kubelka, P.; Munk, F. An article on optics of paint layers. *Z. Tech. Phys.* **1931**, *12*, 259–274.
- (60) Tauc, J.; Grigorovici, R.; Vancu, A. Optical properties and electronic structure of amorphous germanium. *Physica Status Solidi B* **1966**, *15*, 627–637.
- (61) Makuła, P.; Pacia, M.; Macyk, W. How to correctly determine the band gap energy of modified semiconductor photocatalysts based on UV–Vis spectra. 2018.
- (62) Fritsch, V.; Hemberger, J.; Büttgen, N.; Scheidt, E.-W.; von Nidda, H.-A. K.; Loidl, A.; Tsurkan, V. Spin and orbital frustration in MnSc_2S_4 and FeSc_2S_4 . *Physical Review Letters* **2004**, *92*, 116401.
- (63) Tristan, N.; Zestrea, V.; Behr, G.; Klingeler, R.; Büchner, B.; von Nidda, H. K.; Loidl, A.; Tsurkan, V. Spin frustration and magnetic exchange in cobalt aluminum oxide spinels. *Physical Review B* **2008**, *77*, 094412.
- (64) Ghara, S.; Ter-Oganessian, N.; Sundaresan, A. Linear magnetoelectric effect as a signature of long-range collinear antiferromagnetic ordering in the frustrated spinel CoAl_2O_4 . *Physical Review B* **2017**, *95*, 094404.
- (65) Plumb, K.; Morey, J.; Rodriguez-Rivera, J.; Wu, H.; Podlesnyak, A.; McQueen, T.; Broholm, C. Antiferromagnetic and Orbital Ordering on a Diamond

Lattice Near Quantum Criticality. *Physical Review X* **2016**, 6, 041055.

TOC Graphic

